Revision 1

Structure and titanium distribution of feiite characterized using synchrotron single-crystal X-ray diffraction techniques

Claire Zurkowski,[a] Barbara Lavina,[b, c] Kelsey Prissel,[a†] Stella Chariton,[b] Vitali B. Prakapenka[b] and Yingwei Fei[a]

[a]Earth and Planets Laboratory, Carnegie Institution for Science, 5241 Broad, Branch Road, NW, Washington, DC 20015, USA, [b]Center for Advanced Radiation Sources, University of Chicago, 9700 South Cass Avenue, Building 434A, Argonne, IL 60439, USA, [c]X-ray Science Division, Advanced Photon Source, Argonne National Laboratory, Argonne, IL 60439, USA
†Now at: Jacobs, NASA Johnson Space Center, Houston, TX 77058, USA

2

3   Correspondence e-mail: czurkowski@carnegiescience.edu

4

7

8   **Abstract**

9   A solid solution of the mineral feiite (Fe_3TiO_5) was recently discovered in a shock-

10   induced melt pocket of the Shergotty Martian shergottite. It is particularly interesting for its

11   potential as an indicator of pressure-temperature (*P-T*) and oxygen fugacity in Martian crustal

12   and mantle material. To date, complete crystallographic analysis of feiite has not been

13   conducted, as the mineral was previously analyzed by electron back-scatter diffraction on

14   micron-size grains (Ma et al. 2021). Here we report a convergent crystal-structure model for

15   feiite based on synchrotron single-crystal X-ray diffraction data collected on three grains of feiite

16   synthesized at 12 GPa and 1200 ° C. Feiite adopts the $CaFe_3O_5$ structure type (*Cmcm*, *Z* =4)

17   which is composed of two octahedral *M*1 and *M*2 sites and one trigonal prismatic *M*3 site (*M-*

18   =metal) in a ratio of 1:2:1. The three feiite grains with composition $Ti_{0.46-0.60}Fe_{3.54-3.40}O_5$ were

19   best modeled by substituting Ti^{4+} into only the octahedral *M*2 site, accounting for 30% of this

20   site. Comparisons of the measured average bond lengths in the coordination polyhedra with the

21   optimized $Ti^{4+}-O$, $Fe^{2+}-O$, and $Fe^{3+}-O$ bond lengths suggests that ferrous iron occupies the

22 trigonal $M3$ site, while iron is mixed valence in the octahedral $M1$ and $M2$ sites. The Ti^{4+} and

23 Fe^{3+} content constrained by our crystal-chemical analyses suggest that at least ~30% of the

24 available iron must be ferric (i.e., $Fe^{3+}/Fe_{total} = 0.3$) for the sample synthesized at 12 GPa and

25 1200˚ C and higher P-T conditions may be needed to form the endmember feiite ($Fe^{2+}_3TiO_5$).

26

27 **Introduction**

28 The compositions of coexisting iron-titanium-oxides found in terrestrial and

29 extraterrestrial rocks have been established as important indicators of oxygen fugacity in

30 processes including melt crystallization and high P-T impact (e.g., Buddington and Lindsley,

31 1964; Troplis and Carol 1995; Herd et al. 2001). Previous studies have predominantly explored

32 the geochemical and thermodynamic properties of the hematite-ilmenite and magnetite-

33 ulvöspinel (Fe_2TiO_4) series (e.g., Buddington and Lindsley 1964; Ghiorso and Sack 1991; Brown

34 et al. 1993; Ghiorso and Evans 2008; Pearce et al. 2010; Lilova et al. 2012); however, a new

35 (Fe,Ti)-oxide solid solution between feiite (Fe_3TiO_5) and Fe_4O_5 was recently discovered in a

36 shock-induced melt pocket of the Shergotty Martian Shergottite coexisting with $FeTiO_3$ (Ma *et*

37 *al.* 2021), adding new complexities to these geochemical tracers in relation to shocked processes.

38 Experimentally, feiite solid solutions with compositions $Fe_{3.5}Ti_{0.5}O_5$ have been synthesized

39 between 7 and 12 GPa at 1200° C (Prissel *et al.* 2022), supporting that feiite is a high pressure-

40 temperature (P-T) product of Martian impact processes. Examination of the structural and

41 electronic properties of feiite, including the Ti site occupancy, range of Ti solubility, and valence

42 of iron in the structure with pressure and temperature is needed for future application of feiite

43 mineralogy as a P-T-fO_2 tracer of impact processes on Mars.

44   In the Fe-Ti-oxides such as ilmenite and ulvöspinel, Ti^{4+} and Fe^{2+} substitute for 2 Fe^{3+}

45   such that these endmember phases consist of only ferrous iron. Titanium occupies 6-fold

46   coordination with oxygen in these phases. Ilmenite, $FeTiO_3$, consists of alternating layers of

47   FeO_6 and TiO_6 octahedra and ulvöspinel, Fe_2TiO_4, consists of FeO_4 tetrahedra and $(Fe, Ti)O_6$

48   octahedra. Endmember feiite, $(Fe^{2+})_3TiO_5$, based on electron back-scatter diffraction analyses of

49   natural feiite grains from Shergotty (Ma et al. 2021), is assumed to adopt the $CaFe_3O_5$ structure

50   (space group-type *Cmcm*) (Evrard 1980; Ma et al. 2018; 2021), isostructural with Fe_4O_5 (Lavina

51   *et al.* 2011). This structure consists of only 6-fold coordinated sites with a 3:1 ratio of octahedral

52   to trigonal prismatic polyhedra (Evrard, 1980). The $CaFe_3O_5$ structure has been found to

53   accommodate other 2+ cations including Mg, Co, Cr, Ni, Fe, and Mn in a variety of cation

54   distributions (Trots et al. 2012; Woodland et al. 2013; Guignard and Crichton, 2014; Boffa

55   Ballaran et al. 2015; Ovsyannikov et al. 2016; Hong *et al.* 2018a, b, c; Uenver *et al.* 2018; Hong

56   et al. 2022). In general, the largest 2+ cation occupies the trigonal site and the octahedral sites

57   host mixed-valence 2+ and 3+ cations; however, Ti presents a different case as it is a 4+ cation

58   that is significantly smaller than Fe^{2+} in 6-fold coordination (Shannon 1976; O'Niell and

59   Navrotsky 1983; Lavina et al. 2002).

60   It remains unknown how titanium is distributed into this structure and the degree of

61   ordering among Fe and Ti coordination polyhedra. Additionally, recent attempts to synthesize

62   feiite have only been successful in forming a $TiFe_3O_5$-Fe_4O_5 solid solution, and the natural grains

63   of feiite found in Shergotty also contain significant amounts of ferric iron (Ma et al. 2021; Prissel

64   et al. 2022). This suggests that the Fe^{3+} content in feiite may link to the formation conditions.

65   Here we report convergent crystal-structure models for three grains of feiite recovered from 12

66   GPa and 1200° C synthesis conditions based on diffraction data collected using single-crystal

67   synchrotron X-ray diffraction techniques. The distribution of Ti^{4+}, Fe^{2+} and Fe^{3+} are proposed

68   based on the refined site occupancies and average interatomic distances in the refined

69   coordination polyhedra. Limitations on the solubility of Ti^{4+} and the necessity for ferric iron in

70   this structure at relevant *P-T* synthesis conditions are identified and discussed. Results from this

71   work present novel crystallographic insight on Ti substitution into Fe_4O_5 and provide important

72   clues for the formation environments of feiite as an oxythermobarometric marker and

73   geochemical tracer at high pressure-temperature conditions.

74

2. Methods

2.1 Feiite synthesis

77   The feiite crystals examined in this study were synthesized using the multi-anvil press at

78   Carnegie Institution for Science, Earth and Planets Laboratory. Further details of the multi-anvil

79   synthesis are discussed in depth in the related publications by Prissel et al. (2022a, b). The

80   starting material was mixed from FeO (Alfa Aesar 99.5%), Fe_2O_3 (Alfa Aesar 99.9%), and TiO_2

81   (Alfa Aesar 99.99%) with a target composition of 60% Fe_3TiO_5 and 40% Fe_4O_5. This sample

82   was compressed in a 14/8 multi-anvil assembly to 12 GPa. Pressure was calibrated based on the

83   garnet-to-perovskite transition in $CaGeO_3$ at 6 GPa and the coesite-to-stishovite transition in

84   SiO_2 at 9 GPa (Bertka & Fei 1997). At the target pressure, the sample was resistively heated to

85   1200° C and held at high *P-T* for 12.7 hours. Temperature was measured using a Type C

86   thermocouple. . Upon temperature quenching and decompression, the recovered capsules were

87   polished to expose the feiite sample. Electron microprobe chemical analysis for Fe, Ti, Mg and

88   O in backscatter mode was collected on the polished capsules using the JEOL JXA-8530F

89   electron microprobe at Carnegie Earth and Planets Laboratory. Results from these analyses

Revision 1

90   indicate a $Fe_{3.49(2)}Ti_{0.51(1)}O_5$ composition, and further details can be found in the related

91   manuscript (Prissel et al. 2022a, b).

92   *2.2 Collection and processing of synchrotron single-crystal data*

93   Synchrotron X-ray diffraction measurements of the feiite grains were collected at Sector

94   13 BM-D GeoSoilEnviroCARS of the Advanced Photon Source, Argonne National Laboratory.

95   A 42 keV X-ray beam with a spot size of 5 μm x 8 μm full width half maximum was used, and

96   diffracted X-rays were collected with a CdTe 1M Pilatus detector. Diffraction from a LaB_6 NIST

97   standard was used to calibrate the sample-detector geometry, and a single crystal of an

98   orthoenstatite (*Pbca*) with composition and parameters: $(Mg_{1.93}Fe_{0.06})(Si_{1.93}Al_{0.06})O_6$,, a =

99   18.2391(3), b = 8.8117(2), and c = 5.18320(10) Å), was used to calibrate the instrument model in

100   the CrysAlisPro single-crystal software. The feiite samples were rotated +/-50° in the path of the

101   X-ray beam in 0.5° steps with 4s exposure times per step. Using CrysAlis Pro (Rigaku OD),

102   three grains of feiite were indexed and isolated in the reciprocal space and the reflection

103   intensities for each grain were integrated and reduced. The cell parameters and reduced structure

104   factors for the target grains were then input into the ShelxT direct methods structure solution

105   algorithm (Sheldrick, 2015a) to determine a starting structure model.

106

107   *2.3 Structural refinement of feiite*

108   The structure models were then refined by parameterizing the atomic coordinates,

109   displacement parameters, and metal site occupancies using ShelXl2014/7 (Sheldrick, 2014;

110   2015b). As the site occupancies of Ti in the structure were not known initially, refinement of the

111   atomic coordinates and isotropic displacement parameters was first conducted assuming a Fe_4O_5

112   composition. Then, structure models were refined for various Ti configurations: Ti in only one of

113   the metal sites, Ti in only the octahedral sites, and finally, Ti in all the sites. The metal sites were

114   refined anisotropically while maintaining a suitable ratio of observed reflections to refined

115   parameters (Hamilton, 1965). Few outlying reflections exhibiting anomalous calculated-versus-

116   observed intensities, likely due to grain overlap or parasitic scattering, were omitted. Results

117   from the refined structure models for the three grains in each of the (Fe, Ti)-site configurations

118   were then compared (Table S1). The final feiite structure model that was chosen exhibited

119   consistent stoichiometries across the three grains and compatible compositions with the electron

120   microprobe measurements of the synthesized feiite (Prissel et al. 2022a, b). The structure model

121   visualizations presented here were made using Vesta (Momma and Izumi, 2011).

122   **3. Results**

123   The lattices of three grains of feiite were identified in the reciprocal space and indexed to

124   *C*-centered orthorhombic cells (Figure 1). Unit-cell parameters measured on Crystal 1, for

125   example, equal: $a = 2.9268(7)$ Å, $b = 9.8181(15)$ Å, and $c = 12.592(9)$ Å, with $V = 361.8(3)$ Å^3

126   and similar values were measured on Crystal 2 and Crystal 3 (Table S1). Assessment of the

127   systematic absences constrains a *Cmcm* space group (Figure 1).

128   Structural solutions output a starting Fe_4O_5 structure model in agreement with Lavina et

129   al. (2011). Refinement of this structure model was carried out against 203-259 merged

130   reflections for each grain (Table S1). Five Ti distribution models were tested on the data (Table

131   S2), and resolute refinements showing consistency in composition for the three feiite crystals

132   compared to the microprobe analyses of the synthetic sample (Prissel et al., 20022a, b) were

133   obtained with Fe fully occupying the *M*1 and *M*3 sites and both Fe and Ti occupying the

134   octahedral *M*2 site (Figure 2). Iron contents in the octahedral *M*2 site range from 0.70(2) -

135   0.77(2) (Figures 2 and 3), and the stoichiometries determined from the refined structure models

136   are generally described by $Ti_{0.46-0.60}Fe_{3.54-3.40}O_5$ (Table S1). This is in good agreement with the

137   composition of the sample: $Ti_{0.51(1)}Fe_{3.49(2)}O_5$, determined from electron microprobe analyses

138   (Prissel et al. 2022a, b). The statistics of the structure refinements of the three grains using this

139   model are shown in Table 1 with final R_1 = 4.0 - 6.6%, metal U_{equiv} values ranging from

140   0.0129(7) $Å^2$ – 0.018(1) $Å^2$, and oxygen U_{iso} values range from 0.012(1) $Å^2$ – 0.019(2) $Å^2$.

141   Reasonable refinements were also obtained by allowing Ti to dissolve into both

142   octahedral sites (Table S2), but the resultant compositions of the three grains diverged from each

143   other and diverged from the chemical compositions measured on the sample (Prissel et al.,

144   2022). Furthermore, Ti shows a preference to occupy the $M2$ site, as it will not occupy the $M1$

145   site alone, and the refinement statistics did not significantly improve when applying this

146   configuration to the dataset (Table S2). Therefore, while some Ti may disorder into both

147   octahedral sites, predominant occupancy of Ti in the $M2$ site best describes the data, and the

148   details of this structure model will be discussed herein.

149   The M–O interatomic distances measured across the three feiite grains are provided in

150   Table 2 and Figure 3 and show compatible values across three grains. The $M1$ site is coordinated

151   laterally by 4 O4 sites and axially by 2 O5 sites with distances ranging from 2.017(7) Å –

152   2.106(3) Å. The $M2$ site ($Fe_{0.70-0.77}Ti_{0.30-0.23}O_6$) is more distorted and coordinated laterally to 2

153   O4 sites and 2 O5 and axially by one O4 and one O6 site with bond lengths ranging from

154   1.938(5) Å – 2.255(10) Å. The $M3$ trigonal prismatic site is symmetrically capped by 2 O5 at

155   2.234(5) Å and 1 O6 at 2.109(4) Å forming isosceles triangular faces (Figure 2, 3).

156   The grains of feiite used in this study have compositions with approximately 50% Fe_4O_5

157   component (Prissel et al. 2022b), equating to ~25% Fe^{3+} in the structure. In agreement with these

158   chemical analyses, the crystal structure refinements presented indicate 40-54% Fe_4O_5 solid

159   solution. The average interatomic distances in the $M1$, $M2$, and $M3$ sites for the three feiite grains

160   (Table 1) were then used to estimate the occupancies of Fe^{2+}, Fe^{3+}, and Ti^{4+} by determining the

161   linear combination of the cationic species in each site that best matches the average site bond

162   distance (e.g., O'Niell and Navrotsky 1983; Lavina et al., 2002). Cation-oxygen bond lengths for

163   Fe^{2+}, Fe^{3+}, and Ti^{4+} optimized for spinels were used, wherein 6-fold coordination with oxygen,

164   average high-spin (hs) $Fe^{2+} – O$, hs-$Fe^{3+} – O$, and $Ti^{4+} – O$ interatomic distances equal 2.150(2) Å,

165   2.025(1) Å, and 1.962(1) Å, respectively (Lavina et al., 2002).

166   Table 2 shows the estimations of cation distribution for the three grains examined. Taking

167   Crystal 1 as an example, the Ti content was refined in the structure model to 0.46 atoms per

168   formula unit (apfu). This equates to a 54% Fe_4O_5 solid solution and fixes the Fe^{2+} and Fe^{3+}

169   abundances to 2.46 and 1.08 apfu, respectively. The $M3$ trigonal site contains the longest average

170   M–O distance of 2.192(5) Å suggesting that this site is comprised of ferrous iron (Table 1). The

171    $M2$ octahedral site has a fixed 23% Ti component, a multiplicity of 2, and an average M–O

172   distance of 2.077(4) Å. A contribution of 52% Fe^{2+} and 24% Fe^{3+} in this site best matches the

173   average bond length. The remaining ferric and ferrous iron is distributed into the $M1$ octahedral

174   site with the resulting proportions of 40% Fe^{2+} and 60% Fe^{3+} matching an average bond length of

175   2.076(4) Å. Applying this to the other two crystals examined, the approximated feiite cation

176   distributions are in the range: $^{M3}(Fe^{2+})\,^{M2}(Ti^{4+}_{0.23-0.30}Fe^{3+}_{0.10-0.24}Fe^{2+}_{0.53-0.60})_2\,^{M1}(Fe^{3+}_{0.60}Fe^{2+}_{0.40})$

177   O_5, showing excellent compatibility among the three grains examined and the chemical analyses

178   from Prissel et al. (2022b) (Table 3).

179

180   4. **Discussion**

Revision 1

181   In the grains examined in this study, Ti^{4+} has a site preference for the *M*2 octahedral site

182   with maximum occupancy of 0.60 afpu, such that the solubility of Fe_3TiO_5 into Fe_4O_5 is limited

183   to 60 % and 20-30% of the available iron must be ferric to stabilize feiite at 12 GPa and 1200 ˚C.

184   Natural feiite grains found in Shergotty also contain significant amounts of ferric iron

185   corresponding to an approximate 20% Fe_4O_5 component (Ma et al. 2021). Recent experimental

186   exploration confirms that formation of the feiite structure between 7 – 12 GPa and to 1200 ˚C

187   requires a minimum of ~25 % Fe^{3+} (Prissel et al., 2022a, b). Forming endmember Fe_3TiO_5,

188   composed of solely ferrous iron, may therefore require higher *P-T* synthesis conditions.

189   Other (Fe, Ti)-oxides systems, such as the Fe_2O_3 – $FeTiO_3$ and Fe_3O_4 – Fe_2TiO_4 systems

190   exhibit complete solid solutions at high *P-T*, and Ti dissolves into the octahedral sites in the

191   Fe_4O_5 – Fe_3TiO5, Fe_2O_3 – $FeTiO_3$, and Fe_3O_4 – Fe_2TiO_4 solutions (e.g., Brown et al. 1993;

192   Harrison and Redfern 2001; Bosi et al. 2009; Pearce et al. 2010; Lilova et al. 2012; Yamanaka et

193   al. 2013). The behavior of Ti^{4+} in Fe_2O_3 and Fe_3O_4 may therefore provide insight on the role of

194   *P-T* in forming endmember feiite. In the Fe_2O_3 and Fe_3O_4 systems, complete solution of Ti to

195   form $FeTiO_3$ and Fe_2TiO_3 occurs at high temperatures, but the distribution of Ti^{4+} between the

196   octahedral sites differs. For the Fe_3O_4 - Fe_2TiO_4 system, Ti dissolves into both octahedral sites

197   continuously with temperature (Lilova et al. 2012). In the Fe_2O_3 - $FeTiO_3$ system, Ti^{4+} orders

198   into one of the octahedral layers irrespective of temperature for high Ti contents (Brown et al.

199   1993). For lower Ti contents, Ti remains ordered into one of the layers at low temperatures, and

200   disorders among the two layers at high temperatures (Brown et al. 1993). In the grains analyzed

201   in this study, Ti prefers to occupy one of the octahedral sites (*M*2 site) in the Fe_4O_5 structure, but

202   the Ti occupancy in this site is limited. The behavior of both the magnetite–ulvöspinel and

203   ilmenite–hematite solutions supports that temperature is likely a viable mechanism to increase Ti

204   occupancy in the octahedral sites either by expanding the Ti occupancy in the $M2$ site or by

205   incorporating Ti into the $M1$ and $M2$ sites. Considering the behavior of the hematite – ilmenite

206   system, for limited Ti contents in the structure as is observed in this study, increasing

207   temperature may be particularly important for promoting Ti occupancy in the other octahedral

208   site ($M1$) to form endmember feiite.

209   Regarding the pressure effects on titanium distribution in the Fe_4O_5 structure, electronic

210   spin transitions in iron at higher pressures may facilitate complete solid solution and formation of

211   endmember feiite. Due to the octahedral site multiplicities in the feiite structure, an Fe_3TiO_5

212   compound can only be achieved with Ti partially occupying the octahedral sites. With this,

213   minimizing the size difference between ferrous iron and titanium may be critical for forming the

214   feiite endmember. At ambient conditions, octahedrally coordinated Ti^{4+}, high-spin (hs) Fe^{2+} and

215   low spin (ls) Fe^{2+} ionic radii equal 0.605 Å, 0.78 Å, and 0.61 Å, respectively (Shannon, 1976).

216   Therefore, the cationic radii of low-spin ferrous iron and titanium are significantly closer in size

217   compared to the hs state, and this size difference will continue to diminish with pressure. With

218   increasing pressure, a $hs – ls$ transition in Fe^{2+} has been observed to initiate around 14 GPa in

219   Fe_2TiO_4, and Fe^{2+} is observed to undergo this transition more readily in the octahedral versus

220   tetrahedral sites (Yamanaka et al. 2013). Additionally, analogous structural transitions observed

221   in Fe_3O_4 are observed at approximately 10 GPa lower pressures in Fe_2TiO_4 and are facilitated by

222   the $hs – ls$ transition in Fe^{2+} in the octahedral sites (Yamanaka et al. 2013). These results suggest

223   that increasing pressure is a viable mechanism for facilitating the shared site occupancy of Ti and

224   ls Fe^{2+} in the octahedral sites, leading to the formation of endmember feiite. Incorporation of Ti

225   may also provoke phase transitions in Fe_4O_5 at significantly lower pressures and provide another

226   important tracer of the P-T history in the host materials.

Revision 1

227

228

5. Implications

230   The current study supports recent reports that feiite will only form from oxidized host

231   materials between 7 – 12 GPa and 1200 ˚C (Prissel et al. 2022a, b), and specifies that at least ~

232   20-30% of the available iron in the host material must be ferric under the synthesis conditions.

233   However, consideration of the possible pressure and temperature effects on Ti distribution in

234   Fe_4O_5 suggests that increasing pressure and temperature may facilitate the formation of end-

235   member feiite (Fe_3TiO_5) and therefore the formation of the more reduced phase. At more

236   extreme conditions, the stability of feiite may act as a buffer to form reduced phase assemblages.

237   While meteoritic materials such as Shergotty are oxidized with ~ $\Delta IW+2$ and are therefore

238   compatible with the formation of the (Fe, Ti)$_4$O$_5$ solid solution described here, shergottites such

239   as QUE 94201 and other meteoritic materials including aubrites, eucrites, and lunar samples are

240   likely too reducing to form the $Fe_{3.5}Ti_{0.5}O_5$ composition at the same shock conditions (e.g., Sato

241   et al. 1973; Wadhwa 2008 and references therein). With more extreme shock conditions, it is

242   possible that increasingly reduced (Fe, Ti)$_4$O$_5$ grains may form and the endmember compound

243   may be achieved. This possibility necessitates further experiments exploring the Ti distribution

244   and oxidation of the Fe_4O_5 – Fe_3TiO_5 solid solution series as a function of pressure and

245   temperature to establish this system as an oxythermobarmoeter of planetary impact processes.

246   The potential correction between pressure-temperature condition and Ti solubility would also be

247   useful indicator for formation environment of possible terrestrial feiite that may exists in the

248   mantle rocks such as deep diamond inclusions.

249

Revision 1

250

251

260

261

262

263

References

265   Baur, W. H., 1974 The geometry of polyhedral distortions. Predictive relationships for the
266   phosphate group. Acta Crystallographica Section B: Structural Crystallography and
267   Crystal Chemistry, 30, 1195.
268   Bertka, C.M., and Fei, Y., 1997. Mineralogy of the Martian interior up to core-mantle boundary
269   pressures. Journal of Geophysical Research: Solid Earth, 102, 5251–5264.
270   Boffa Ballaran, T., Uenver-Thiele, L., and Woodland, A.B., 2015. Complete substitution of Fe^{2+}
271   by Mg in Fe_4O_5: The crystal structure of the $Mg_2Fe_2O_5$ end-member. American
272   Mineralogist, 100(2-3), 628-632.
273   Buddington, A.F., and Lindsley, D.H. (1964) Iron-titanium oxide minerals and synthetic
274   equivalents. Journal of Petrology, 5(2), 310-357.
275   Cassidy, S.J., Orlandi, F., Manuel, P. and Clarke, S.J., 2019. Single phase charge ordered
276   stoichiometric $CaFe_3O_5$ with commensurate and incommensurate trimeron ordering.
277   Nature communications, 10(1), 1-10.
278   Deng, Z., Moynier, F., Villeneuve, J., Jensen, N.K., Liu, D., Cartigny, P., Mikouchi, T., Siebert,
279   J., Agranier, A., Chaussidon, M. and Bizzarro, M., 2020. Early oxidation of the Martian
280   crust triggered by impacts. Science Advances, 6(44), p.eabc4941.

Revision 1

281 Evrard, O., Malaman, B., Jeannot, F., Courtois, A., Alebouyeh, H. and Gerardin, R., 1980. Mise
282   en évidence de $CaFe_4O_6$ et détermination des structures cristallines des ferrites de
283   calcium $CaFe_{2+n}O_{4+n}$, (n= 1, 2, 3): nouvel exemple d'intercroissance. Journal of Solid
284   State Chemistry, 35, 112.
285 Farges, F. and Brown Jr, G.E., 1997. Coordination chemistry of titanium (IV) in silicate glasses
286   and melts: IV. XANES studies of synthetic and natural volcanic glasses and tektites at
287   ambient temperature and pressure. Geochimica et Cosmochimica Acta, 61(9),1863-1870.
288 Fei, Y., Zhang, L., Corgne, A., Watson, H., Ricolleau, A., Meng, Y. and Prakapenka, V., 2007.
289   Spin transition and equations of state of (Mg, Fe) O solid solutions. Geophysical
290   Research Letters, 34(17).
291 Gagné, O.C. and Hawthorne, F.C., 2020. Bond-length distributions for ions bonded to oxygen:
292   results for the transition metals and quantification of the factors underlying bond-length
293   variation in inorganic solids. IUCrJ, 7(4), pp.581-629.
294 Ghiorso, M.S., and Evans, B.W. (2008). Thermodynamics of rhombohedral oxide solid solutions
295   and a revision of the Fe-Ti two-oxide geothermometer and oxygen-barometer. American
296   Journal of science, 308(9), 957-1039.
297 Ghiorso, M. S., and Sack, O. (1991). Fe-Ti oxide geothermometry: thermodynamic formulation
298   and the estimation of intensive variables in silicic magmas. Contributions to Mineralogy
299   and Petrology, 108(4), 485-510.
300 Guignard, J., and Crichton, W.A. (2014) Synthesis and recovery of bulk Fe_4O_5 from magnetite,
301   Fe_3O_4. A member of a self-similar series of structures for the lower mantle and transition
302   zone. Mineralogical Magazine, 78, 361–371.
303 Hamilton, W.C., 1965. Significance tests on the crystallographic R factor. Acta
304   Crystallographica, 18(3), 502-510.
305 Herd, C.D., Papike, J.J. and Brearley, A.J., 2001. Oxygen fugacity of martian basalts from
306   electron microprobe oxygen and TEM-EELS analyses of Fe-Ti oxides. American
307   Mineralogist, 86(9), 1015-1024.
308 Hong, K.H., Arevalo-Lopez, A.M., Cumby, J., Ritter, C. and Attfield, J.P., 2018a. Long range
309   electronic phase separation in $CaFe_3O_5$. Nature communications, 9(1), 1-6.
310 Hong, K.H., Arevalo-Lopez, A.M., Coduri, M., McNally, G.M. and Attfield, J.P., 2018b. Cation,
311   magnetic, and charge ordering in $MnFe_3O_5$. Journal of Materials Chemistry C, 6(13),
312   3271-3275.
313 Hong, K.H., Solana-Madruga, E., Coduri, M. and Attfield, J.P., 2018c. Complex Cation and Spin
314   Orders in the High-Pressure Ferrite $CoFe_3O_5$. Inorganic chemistry, 57(22), 14347-14352.
315 Hong, K., Solana, E., Coduri, M., Ritter, C. and Attfield, P., 2022. Synthesis, Structure and
316   Magnetic Properties of $NiFe_3O_5$. ECS Journal of Solid State Science and Technology.
317 Lavina, B., Salviulo, G. and Giusta, A.D., 2002. Cation distribution and structure modelling of
318   spinel solid solutions. Physics and Chemistry of Minerals, 29(1), 10-18.
319 Lavina, B., Dera, P., Downs, R.T., Prakapenka, V., Rivers, M., Sutton, S. and Nicol, M., 2009.
320   Siderite at lower mantle conditions and the effects of the pressure-induced spin-pairing
321   transition. Geophysical Research Letters, 36(23).
322 Lavina, B., Dera, P., Kim, E., Meng, Y., Downs, R.T., Weck, P.F., Sutton, S.R., and Zhao, Y.
323   2011. Proceedings of the National Academy of Sciences, 108, 17281–17285.
324 Lin, J.F., Gavriliuk, A.G., Struzhkin, V.V., Jacobsen, S.D., Sturhahn, W., Hu, M.Y., Chow, P.
325   and Yoo, C.S., 2006. Pressure-induced electronic spin transition of iron in
326   magnesiowustite-(Mg, Fe) O. Physical Review B, 73(11), 113107.

327   Ma, C. and Tschauner, O., 2018. Feiite, IMA 2017-041a. CNMNC Newsletter No. 46,
328   December 2018, Mineralogical Magazine, 82, 1369–1379.
329   Ma, C., Tschauner, O., Beckett, J.R. and Prakapenka, V., 2021, March. Discovery of Feiite
330          $(Fe^{2+}_2(Fe^{2+} Ti^{4+}) O_5)$ and Liuite (GdFeO$_3$-Type FeTiO$_3$), two new shock-induced, high-
331   pressure minerals in the Martian meteorite Shergotty. In Lunar and Planetary Science
332   Conference, No. 2548, 1681.
333   Millet, M.A., Dauphas, N., Greber, N.D., Burton, K.W., Dale, C.W., Debret, B., Macpherson,
334   C.G., Nowell, G.M. and Williams, H.M., 2016. Titanium stable isotope investigation of
335   magmatic processes on the Earth and Moon. Earth and Planetary Science Letters, 449,
336   197-205.
337   Momma, K. and Izumi, F., 2011. VESTA 3 for three-dimensional visualization of crystal,
338   volumetric and morphology data. Journal of Applied Crystallography, 44(6), 1272-1276.
339   Ovsyannikov, S.V., Bykov, M., Bykova, E., Kozlenko, D.P., Tsirlin, A.A., Karkin, A.E.,
340   Shchennikov, V.V., Kichanov, S.E., Gou, H., Abakumov, A.M. & Egoavil, R., 2016.
341   Nature Chemistry, **8**, 501–508.
342   Pearce, C.I., Henderson, C.M.B., Telling, N.D., Pattrick, R.A., Charnock, J.M., Coker, V.S.,
343   Arenholz, E., Tuna, F. and van der Laan, G., 2010. Fe site occupancy in magnetite-
344   ulvospinel solid solutions: A new approach using X-ray magnetic circular dichroism.
345   American Mineralogist, 95(4), 425 – 439.
346   Prissel, K.B., Fei, Y. and Strobel, T.A., 2022a. Synthesis and stability of Feiite with implications
347   for its formation conditions in nature. LPI Contributions, 2678, 1164.
348   Prissel, K.B., Fei, Y. and Strobel, T.A., 2022b. Synthesis and stability of Feiite with
349   implications for its formation conditions in nature. American Mineralogist, *in press*. DOI:
350   10.2138/am-2022-8633.
351   Rigaku Oxford Diffraction, 2021. CrysAlis PRO software system, ver. 1.171.41.115a Rigaku
352   Corporation, Oxford, U.K.
353   Sato, M., Hickling, N.L. and McLane, J.E., 1973. Oxygen fugacity values of Apollo 12, 14, and
354   15 lunar samples and reduced state of lunar magmas. In Lunar and Planetary Science
355   Conference Proceedings, Vol. 4, 1061.
356   Shannon, R.D., 1976. Revised effective ionic radii and systematic studies of interatomic
357   distances in halides and chalcogenides. Acta crystallographica section A: crystal physics,
358   diffraction, theoretical and general crystallography, 32(5), 751-767.
359   Sheldrick, G.M., 2014. SHELXL-2014/7: program for the solution of crystal structures.
360   University of Göttingen, Göttingen, Germany.
361   Sheldrick, G.M., 2015a. SHELXT–Integrated space-group and crystal-structure determination.
362   Acta Crystallographica Section A: Foundations and Advances, 71(1), 3-8.
363   Sheldrick, G.M., 2015b. Crystal structure refinement with SHELXL. Acta Crystallographica
364   Section C: Structural Chemistry, 71(1), 3-8.
365   Toplis, M.J. and Carroll, M.R., 1995. An experimental study of the influence of oxygen fugacity
366   on Fe-Ti oxide stability, phase relations, and mineral—melt equilibria in ferro-basaltic
367   systems. Journal of Petrology, 36(5),1137-1170.
368   Trots, D.M., Kurnosov, A., Woodland, A.B., and Frost, D.J. (2012) The thermal breakdown of
369   Fe$_4$O$_5$ at ambient pressure. European Mineralogical Conference, 1, EMC2012-556-1.
370   Uenver-Thiele, L., Woodland, A.B., Miyajima, N., Ballaran, T.B. and Frost, D.J., 2018.
371   Behavior of Fe$_4$O$_5$–Mg$_2$Fe$_2$O$_5$ solid solutions and their relation to coexisting Mg–Fe
372   silicates and oxide phases. Contributions to Mineralogy and Petrology, 173(3),1-16.

Revision 1

373   Wadhwa, M., 2008. Redox conditions on small bodies, the Moon and Mars. Reviews in
374   Mineralogy and Geochemistry, 68(1), 493-510.
375   Woodland A.B., Schollenbruch K., Koch M., Boffa Ballaran T., Angel R.J., Frost D.J., 2013.
376   Fe_4O_5 and its solid solutions in several simple systems. Contributions to Mineralogy and
377   Petrology,166,1677–1686
378   Yamanaka, T., Kyono, A., Nakamoto, Y., Meng, Y., Kharlamova, S., Struzhkin, V.V. and Mao,
379   H.K., 2013. High-pressure phase transitions of $Fe_{3-x}Ti_xO_4$ solid solution up to 60 GPa
380   correlated with electronic spin transition. American Mineralogist, 98(4), 736-744.

381

382

383

384

385

386

387

388

389

390

391   **Table 1**. Interatomic distances for the octahedral and trigonal prismatic coordination polyhedra
392   measured in the three crystals of feiite.

Bond	Crystal 1			Crystal 2			Crystal 3		
	Distance	Average	Distortion Index	Distance	Average	Distortion Index	Distance	Average	Distortion Index[a]
	(Å)	(Å)		(Å)	(Å)		(Å)	(Å)	
Fe1–O4 (x 4)	2.106(3	2.076(4)	0.0191(2)	2.101(4)	2.075(6)	0.0165(2)	2.104(4)	2.083(6)	0.0135(2)
Fe1–O5 (x 2)	2.017(7)			2.024(10)			2.041(10)		
(Fe, Ti)2–O4 (x 2)	2.071(4)	2.077(4)	0.0282(2)	2.086(5)	2.081(6)	0.0275(3)	2.078(5)	2.080(6)	0.0281(3)
(Fe, Ti)2–O4 (x 1)	2.252(7)			2.244(9)			2.255(10)		
(Fe, Ti)2–O5 (x 2)	2.062(3)			2.067(5)			2.063(4)		
(Fe, Ti)2–O6 (x 1)	1.941(3)			1.938(5)			1.940(5)		
Fe3–O5 (x 4)	2.234(5)	2.192(5)	0.0253(2)	2.230(7)	2.193(7)	0.0223(3)	2.225(7)	2.188(7)	0.023(3)
Fe3–O6 (x 2)	2.109(4)			2.120(7)			2.114(6)		

[a]Distortion indices based on the bond lengths were calculated from Baur (1974).

393

Revision 1

394 **Table 2.** Cation distributions of Fe^{2+}-, Fe^{3+}, Ti^{4+} in the octahedral $M1$ and $M2$ sites tabulated for
395 the three crystals of feiite examined in this study. The cation distributions were estimated by
396 calculating a linear combination of Fe^{2+}-, Fe^{3+}-, Ti^{4+}--O bond lengths from Lavina et al. (2002)
397 that best matched the measured bond lengths for the octahedral $M1$ and $M2$ sites.
398

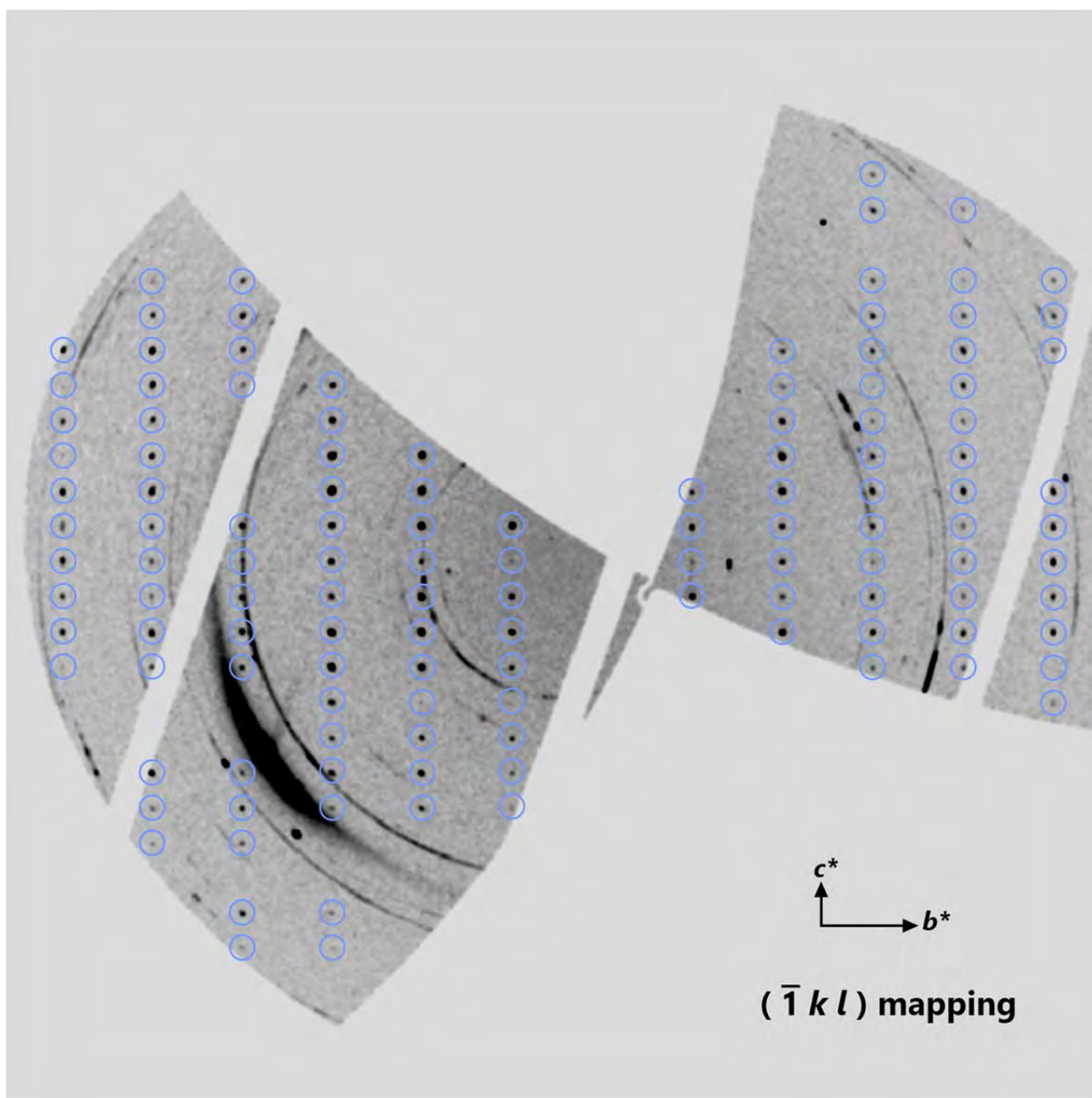| | atomic % in site | | | | | | | | Calculated | | Measured | |
| | M1 | | | 2M2 | | | | M3 | $M1$ bond length (Å) | $M2$ bond length (Å) | $M1$ bond length (Å) | $M2$ bond length (Å) |
	Fe^{2+}	Fe^{3+}	total	Ti^{4+}	Fe^{2+}	Fe^{3+}	total	Fe^{2+}				
Crystal 1	0.4	0.6	1	0.46	1.06	0.48	2	1	2.075	2.077	2.076(4)	2.077(4)
Crystal 2	0.4	0.6	1	0.6	1.2	0.2	2	1	2.075	2.081	2.075(6)	2.081(6)
Crystal 3	0.4	0.6	1	0.48	1.08	0.44	2	1	2.075	2.077	2.083(6)	2.080(6)

399

400

401

402

403

404

405

406

407 **Figure 1.**

Revision 1

409   **Figure 1.** Diffraction reflections (circled in blue) satisfying the condition: -1 *k l* for a feiite
410   crystal. The Debeye rings arise from air scattering on the pinhole and are not related to the
411   sample. A diffraction image collected at the edge of the sample is provided in Figure S1 to
412   demonstrate that the Debeye rings do no change in intensity and are not related to the sample.
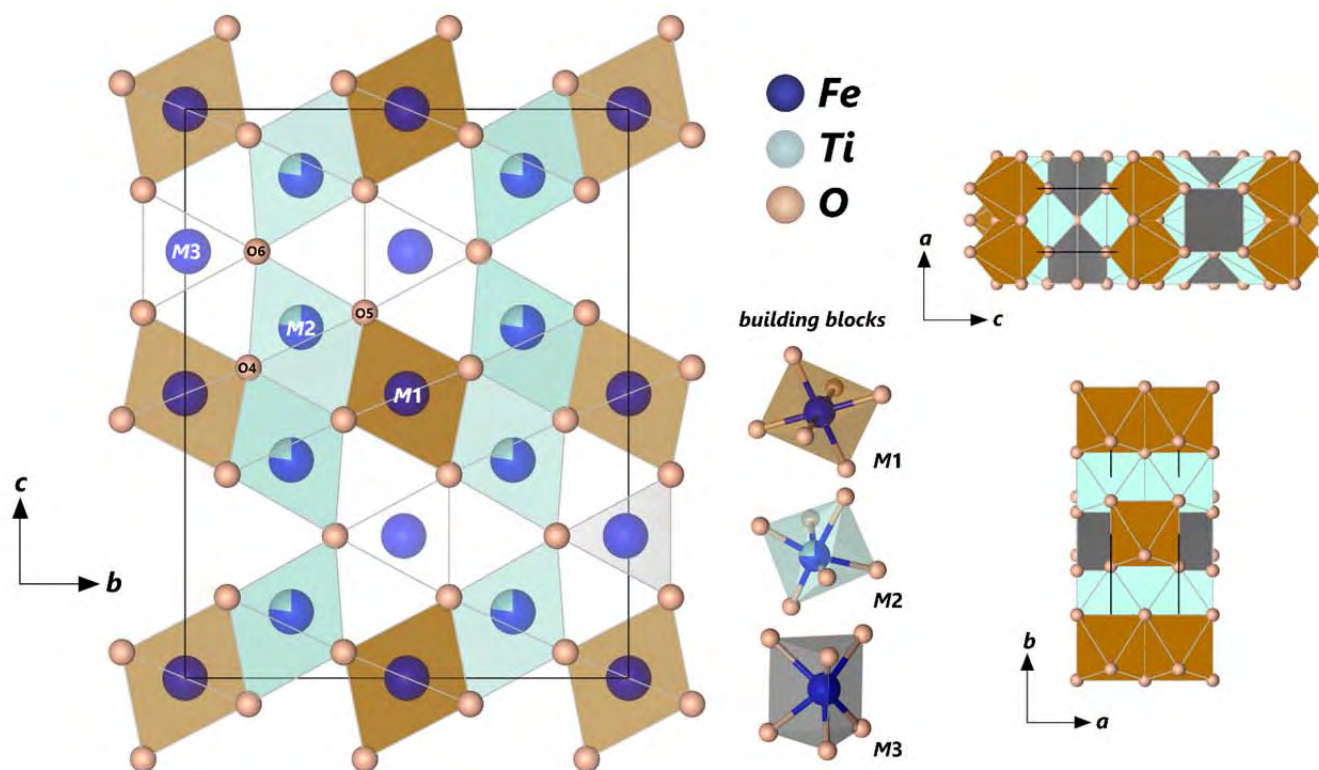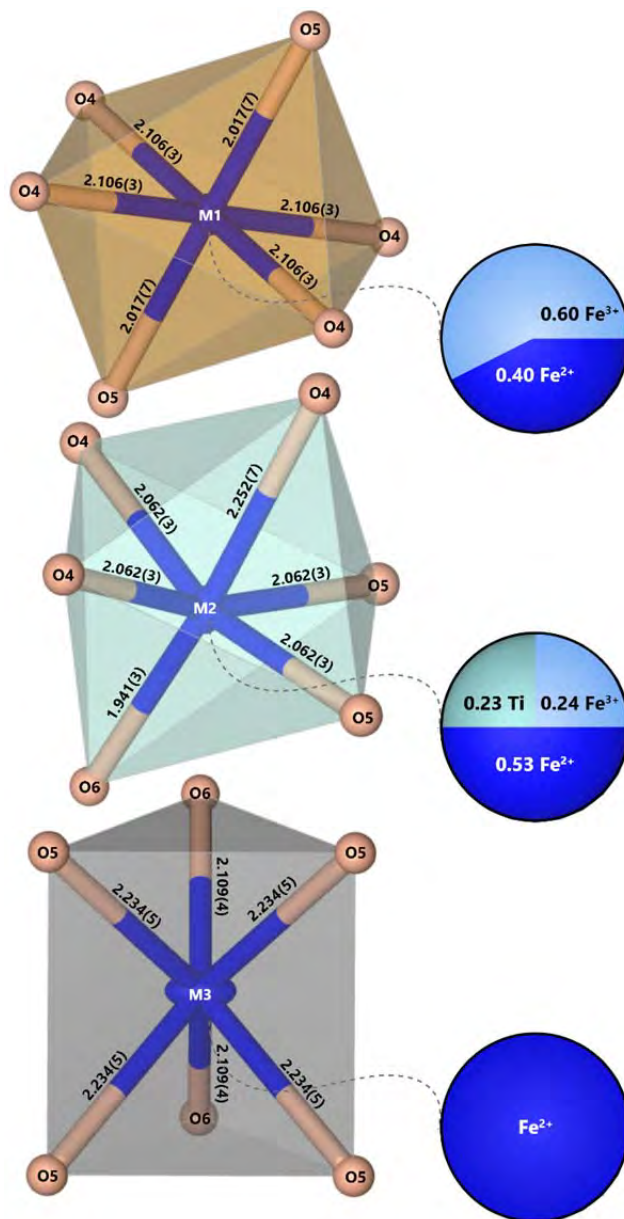
413
414
415
416
417
418
419
420

Revision 1

421   **Figure 2.**

423   **Figure 2.** Crystal structure and chemistry of feiite Crystal 1 with refined composition
424    $Ti_{0.46}Fe_{3.54}O_5$ (Table S1). The asymmetric unit of metal (Fe, Ti) and oxygen sites are labeled. The
425   unit cell consists of consisting of the $M1$ and $M2$ octahedral sites and an $M3$ trigonal site in a
426   ratio of 1:2:1 with ~25% of the $M2$ sites occupied by titanium. The views along the b and c axes
427   illustrate the edge and corner sharing of the polyhedra. The structure is arranged into columns of
428   edge sharing $M1O_6$ octahedra, edge sharing $M2O_6$ octahedra, and face sharing $M3O_6$ bicapped
429   trigonal prisms extending along the a direction. In the b and c directions, the columns of
430   octahedra are joined along edges while the columns of trigonal prims are linked to the columns
431   of octahedra along corners.

432
433
434
435
436
437
438
439
440
441
442
443

444 **Figure 3.**

445
446 **Figure 3.** Bond lengths and site occupancy refined for the MO_6 (M = Fe^{2+}, Fe^{3+}, Ti) sites in
447 Crystal 1. The anisotropic displacement of the metal sites is visualized with 50% probability.
448
449

450

451

452

453